Configuration and model order selection of frequency-dependent π-models for representing dc-cables in small-signal eigenvalue analysis of HVDC transmission systems

Salvatore D'Arco, Jon Are Suul, *Member, IEEE,* Jef Beerten, *Senior Member, IEEE*

Abstract—Eigenvalue-based analysis of small-signal dynamics in High Voltage Direct Current (HVDC) transmission systems requires cable models that are compatible with a state-space representation. While distributed parameter models accounting for frequency-dependent effects are inherently incompatible with a state-space representation, a conventional π-model can only represent the cable behavior accurately at a single frequency. Instead, a Frequency-Dependent π-model (FD-π), consisting of a lumped circuit representation with multiple parallel RL-branches in each π-section can be utilized to reproduce the frequency-dependency of the cable characteristics in a specified frequency range. Based on an evaluation of relevant error metrics for FD-π models, this paper demonstrates how the number of sections and the number of parallel branches in each section will influence the accuracy. From this starting point, an optimization algorithm for identifying the configuration that fulfills specified accuracy requirements with the lowest possible model order is introduced. A similar algorithm for identifying the most accurate FD-π model within a specified maximum model order is also proposed. Numerical results for different cable lengths and cross sections are presented to highlight their effect on the model, and it is demonstrated how the cable model configuration can influence the results from small-signal eigenvalue analysis of an HVDC transmission system.

Index Terms—Cable modeling, HVDC transmission, small-signal eigenvalue analysis, state-space modeling, vector fitting

I. INTRODUCTION

ASSESSING the small-signal dynamics and stability by eigenvalue analysis is common practice for large-scale ac power systems. With the prospect of future multi-terminal High Voltage Direct Current (HVDC) transmission schemes [1], small-signal eigenvalue analysis has been increasingly applied also for studies of cable-based Voltage Source Converter (VSC) HVDC systems [2]–[5]. For this purpose, accurate and linearizable state-space models of each system component are needed to obtain a linear model expressed as $\Delta\dot{\mathbf{x}} = \mathbf{A}\Delta\mathbf{x} + \mathbf{B}\Delta\mathbf{u}$. Suitable models of 2-level (2L) VSC HVDC terminals with conventional control systems are already well established, while models for representing Modular Multilevel Converters (MMCs) have been recently developed [6]–[10]. However, the state-of-the art models for time-domain simulation of HVDC cables, such as the Universal Line Model (ULM) [11], have been specifically developed for time domain simulation by Electro-Magnetic Transient (EMT) software. In general, such models include time-delays and functions that are inherently incompatible with a state-space representation and an eigenvalue-based analysis. Consequently, lumped-parameter models based on classical cascaded π-sections have been commonly used for small-signal analysis of VSC HVDC systems [3], [12]–[15]. However, this approach relies on the implicit assumption that the cable parameters can be considered constant within the frequency range of interest [16].

The accurate representation of the cable dc-resistance is crucial for analysing (low-frequency) oscillations in HVDC systems. Moreover, in long cable systems the dynamics of the HVDC converter terminals can reach the same frequency range as the lowest internal cable resonance frequencies [12], [17]. Therefore, both the the dc-resistance value and the impedance characteristics within a wider frequency range are important for cable modelling. Furthermore, it has been recently demonstrated that traditional cascaded π-section models can generate misleading assessments of the overall system dynamics [17]–[19] since the frequency-dependent characteristics of the HVDC cables are inherently neglected.

Earlier work on transmission system modeling have proved that lumped parameter networks can be specified to match cable parameters over a frequency range by using ladder networks [20]. For instance, ladder-type networks are included in the RTDS real-time simulation library for modelling frequency-dependent inductances and resistances [21]. Even though they are mainly developed for the purpose of time-domain simulations, such lumped parameter models are directly applicable to state-space modelling and eigenvalue-

based analysis. More recently, also dedicated modelling approaches for state-space modelling of HVDC cables have been proposed. For instance, a coupled π-section model intended for representing parts of the frequency-dependent cable characteristics was proposed by [18]. Later, a more general method obtaining a Frequency-Dependent π-model (FD-π) suitable for capturing HVDC cable dynamics in the frequency range of importance for system-oriented small-signal eigenvalue analysis was developed in [4], [22]. The resulting model represents the frequency-dependent characteristics of the cable by utilizing multiple parallel RL-branches in each π-section and its lumped parameter structure ensures a straightforward state-space formulation. Furthermore, it has been validated that FD-π models can provide an accurate representation of the cable dynamics over the entire frequency range from dc to frequencies beyond the bandwidth of the HVDC control system. Thus, the application of FD-π models can significantly improve the representation of the HVDC cable dynamics compared to traditional π-section models and can prevent incorrect predictions of instabilities [19].

The accuracy and validity range of an FD-π model can be adjusted by varying the number of π-sections and the number of parallel branches in each section. However, previous publications introducing and applying FD-π models have only demonstrated the behavior of a few model configurations in specific case studies. As an example, the disturbance attenuation of various dc voltage droop control schemes was evaluated in [23] considering a single section FD-π model. Similarly, the model utilized in [24] is adapted to account for the first resonance peak in the design of converter controllers. In [25], the model was used to evaluate the dynamic performance of an interline flow controller for HVDC grids. Furthermore, the impact of the cable model accuracy on the stability was investigated in [17], but again limited to the analysis of a single FD-π section. A first analysis of how the accuracy of an FD-π model of HVDC cables relates to the model order and the model configuration was presented in [26]. However, no comprehensive analysis of how the model should be configured for fulfilling predefined accuracy requirements is available in literature.

This paper systematically addresses how an FD-π model should be specified for representing HVDC cables in small-signal eigenvalue analysis of HVDC transmission schemes. The analysis from [26] is formalized and further extended to provide a reference for understanding how to configure FD-π models. First, the influence of the number of π-sections and the number of parallel branches on the accuracy of the model is demonstrated in the frequency domain and in the time-domain. Furthermore, it is shown how the model errors are related to the model order for examples of FD-π models with different number of parallel branches. On this basis, the main contribution of the paper is the formulation of an approach for selecting the most suitable FD-π model configuration within a specified frequency range. In particular, two algorithms for identifying the optimal configuration of an FD-π model under a specified set of constraints are proposed:

1) An algorithm for identifying an FD-π model of minimum order according to a desired accuracy requirement within a given frequency range, i.e. minimization of model order under accuracy constraint
2) An algorithm for finding the most accurate FD-π model within a specified frequency range, limited by a maximum model order, i.e. minimization of error under model order constraint.

A numerical tool for generating HVDC cable models with a specific model configuration or by applying the proposed algorithms is also electronically available together with this paper [1].

The paper also includes additional contributions supporting the proposed approach for optimization of FD-π model configurations. Firstly, the analysis leading to the proposed algorithms is based on a systematic evaluation of error metrics and their impact on the model characteristics. Furthermore, the parameter sensitivity of the optimal FD-π models is evaluated by considering a range of cable lengths and various cable cross-sections. These results provide a basis for indicating general guidelines and practical recommendations for selecting suitable model configurations for small-signal analysis of HVDC transmission systems. Finally, examples of eigenvalue-based analysis, supported by time-domain verification, demonstrate how the obtained minimum order FD-π model can accurately represent the cable dynamics for system-oriented studies. Two cases are presented, based on point-to-point HVDC interconnections with 2L VSCs or MMC-based converter terminals. The results serve to illustrate how inaccurate representation of the HVDC cables can cause misleading results from small-signal eigenvalue-based analysis and even lead to false prediction of instability. This serves as a clear illustration of the practical importance of the analysis presented in the manuscript and the proposed methods for selecting the cable model configuration.

II. REFERENCE MODELS FOR HVDC CABLES

High fidelity frequency-dependent models for HVDC cables with distributed parameters are well established in literature, and will be used as a reference for the presented analysis of FD-π models. In the following, a Kron reduction is applied, implicitly assuming an ideal grounding for the armour and sheath along the entire length of the cable. This reduction only applies when the voltages in armour and sheath remain small compared to the conductor voltage [27], which is a realistic assumption for the analysis of small-signal dynamics in HVDC transmission systems. As a consequence, the analytical representation of a subsea cable with three conducting layers (conductor, sheath and armour) reduces to that of an equivalent conductor.

A. Reference cable model in the frequency domain

The behavior of an HVDC cable can be accurately represented in the frequency domain by the equivalent circuit model

---

[1]This numerical tool is included as interactive content of this paper and can be downloaded from http://ieeexplore.ieee.org. The tool and any future updates will also be made available from https://www.sintef.no/fdpi-model and https://www.esat.kuleuven.be/electa/teaching/fdpi-model
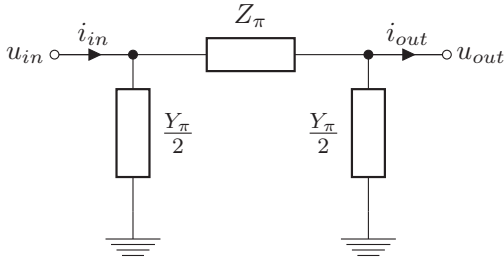
Fig. 1. Exact π representation of HVDC cable

in Fig. 1. The series and shunt elements, $Z_\pi(s)$ and $Y_\pi(s)$ respectively, account for the frequency-dependent characteristics of the cable parameters and for the functional dependency of the impedance with respect to the cable length. These circuit elements can be expressed in the Laplace domain [16], [28], as:

$$Z_\pi(s) = z(s)\,\ell\,\frac{\sinh\gamma(s)\ell}{\gamma(s)\ell}, Y_\pi(s) = y(s)\,\ell\,\frac{\tanh\frac{\gamma(s)\ell}{2}}{\frac{\gamma(s)\ell}{2}} \quad (1)$$

$$\gamma(s) = \sqrt{z(s)y(s)} \quad (2)$$

In (1) and (2), $z(s)$ and $y(s)$ are the cable impedance and admittance per unit length, which also define the propagation constant $\gamma(s)$, while ℓ denotes the cable length. The series impedance $z(s)$ can be expressed as:

$$z(s) = r(s) + s \cdot l(s) \quad (3)$$

where both the longitudinal resistance $r(s)$ and inductance $l(s)$ per unit length are frequency-dependent. It should be noted that the function $z(s)$ is very smooth in the frequency domain and easier to fit with a rational approximation than the function $Z_\pi(s)$. The transverse admittance can be also decomposed as:

$$y(s) = g + s \cdot c \quad (4)$$

In the frequency range of interest for small-signal eigenvalue analysis of HVDC systems, the conductance g and the capacitance c per unit length can be assumed constant [27].

The admittance of the cable terminated on a load impedance $Z_l(s)$ in the Laplace domain can be derived from Fig. 1. Accounting for the expressions in (1)–(2) leads to:

$$Y_c(s) = \frac{\gamma(s)\coth(\gamma(s)l) + y(s)Z_l(s)}{\gamma(s)Z_l(s)\coth(\gamma(s)l) + z(s)} \quad (5)$$

Thus, the behavior of the cable in the Laplace domain is characterized by a frequency-dependent admittance due to presence of the hyperbolic functions and the frequency dependence of the series impedance z. The representation of the cable with $Y_c(s)$ is assumed as a reference model of the cable in the frequency domain.

B. Cable representation in the time-domain

The response of the cable to a unity voltage step applied on u_{in} can be expressed in the Laplace domain as:

$$i_{in}(s) = \frac{Y_c(s)}{s} \quad (6)$$

The response in the time-domain can be obtained numerically via the Inverse Numerical Laplace Transform (INLT). In this paper, results obtained with the INLT implementation presented in [29] are assumed as a reference for the time-domain response of a single cable. Thus, the INLT of (6) with $Y_c(s)$ defined by (5) is used for evaluating the accuracy of the FD-π models in the time-domain.

It can be noted that the INLT is not easily applicable for simulating a complex power system configuration. Therefore, when analyzing complete HVDC transmission schemes including ac-side dynamics and the control of the converter stations, the reference for the time-domain response will be more pragmatically obtained with an ULM as a state-of-the-art model for simulating the cable [11].

III. ANALYSIS OF THE FD-π MODEL

Established EMT modelling approaches (e.g. wide band models or the Bergeron model) are not compatible with a state space representation as necessary for the eigenvalue-based analysis of small-signal dynamics, while traditional cascaded π-section models can accurately represent the cable characteristics only at a single point in the frequency domain. The FD-π model overcomes these two limitations since it is based on a lumped circuit structure that can be easily translated into state space form while also approximating the cable characteristics associated with the frequency dependency of the cable parameters. A general circuit representation of the FD-π model from [19], [22] is shown in Fig. 2. The number of cascaded π-sections n and the number of parallel branches m represent two degrees of freedom in the configuration of a FD-π model. The total model order N for the resulting representation of the cable can be expressed as:

$$N = n \cdot m + n + 1 \quad (7)$$

In the following, the model order N will be utilized as a simplified and pragmatic approach to represent with a single scalar quantity the complexity of the cable model when utilized as part of a larger system. Indeed, a higher model order for the overall system will in general imply a longer time and more memory requirements for the calculation of eigenvalues.

Since the shunt conductance and capacitance of the cable can be assumed constant in the frequency range of interest for system-oriented eigenvalue analysis, their values for each section of the FD-π model can be determined directly according to the length of the cable and the number of π sections n. The values for the longitudinal parameters in the model of Fig. 2 are obtained so that the parallel RL branches can reproduce the frequency-dependence of the series impedance per unit length z, approximated as [22], [28]:

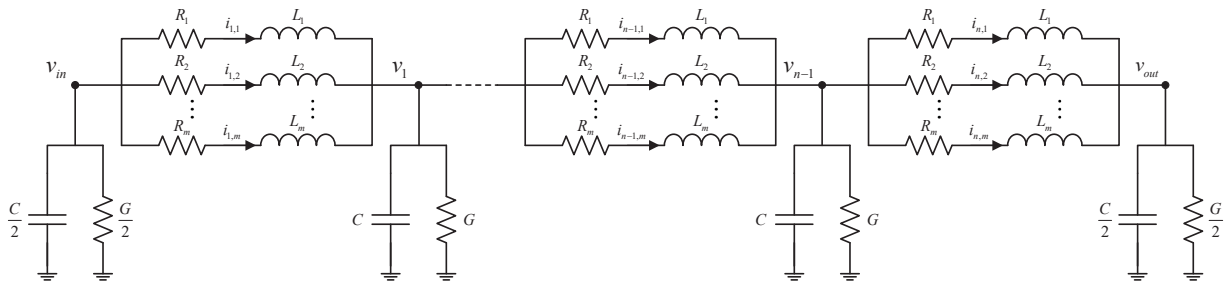$$\frac{1}{z(s)} \approx \sum_{i=1}^{m} \frac{1}{r_i + sl_i} \quad (8)$$

Fig. 2. Circuit representation of the FD-π model

As proposed in [22], the longitudinal parameters for the parallel branches per unit length are determined by applying vector fitting [28], [30]. The parameters of each of the m parallel branches will then result from the cable length and the selected number of π sections.

With a model configuration determined by n and m and the corresponding parameter values, a state-space representation of the FD-π model on the form $\dot{\mathbf{x}} = \mathbf{Ax} + \mathbf{Bu}$ can be easily established directly from the structure shown in Fig. 2, as further explained in [22]. The accompanying numerical tool can generate such models starting from the frequency-dependent cable characteristics[2].

A. Impact of model configuration on accuracy in the frequency- and time-domain

The modeling of a 400 km XLPE HVDC cable with data from [31] is considered in this section as an example for assessing the accuracy of different FD-π model configurations. The ratings and dimensions of the cable are given in Appendix, labelled as Cable 1. For the following analysis it is assumed that the end of the cable is short-circuited. However, as demonstrated by the preliminary investigation in [26], the general characteristics of the results would be similar, with only minor numerical differences, if an open-ended cable was assumed.

In Fig. 3, the frequency characteristics of the reference model from Fig. 1 is compared in amplitude and phase to the impedance of an FD-π model with 10 cascaded sections, for 5 cases with different number of parallel branches. The standard cascaded π-section model ($m = 1$), with parameters chosen to get an accurate dc representation clearly results in a poor representation of the cable resonance frequencies with much less damping than the reference model. Already with $m = 2$, the FD-π model is able to approximately reproduce the 3 to 4 first resonance frequencies. Increasing the number of parallel branches improves the accuracy especially in the range between 10 Hz and 100 Hz. However, the frequency range where the resonances of the reference model are correctly represented remains approximately limited to about 1 kHz. Indeed, all examples consider the same number of FD-π-sections, thereby leading to the same modelling bandwidth. The accuracy appears to increase only marginally when adding more than 5 parallel branches.
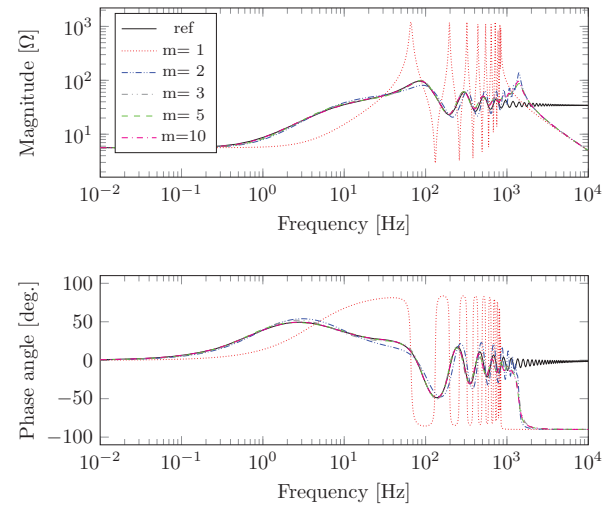
[2]See footnote on page 2.

Fig. 3. Impedance comparison of a 400 km XLPE HVDC cable with $n = 10$ FD-π-sections and varying number of parallel branches m.

The behavior of the FD-π model is compared to the reference model in the time-domain in Fig. 4, where the current i_{in} is displayed for a unity step in the voltage v_{in}. The figure reports also the integral of the absolute error (IAE) defined as:

$$IAE(t) = \int_0^t |i_{in,ref}(\tau) - i_{in,n,m}(\tau)| d\tau \tag{9}$$

The FD-π models with $m \geq 2$ are generally accurate in reproducing the transient behavior in the first milliseconds after a perturbation and the steady-state response or any slowly varying dynamics remaining after several seconds. However, the number of parallel branches is critical for obtaining an accurate representation in the time range between 0.1 and 1.5 s after the perturbation.

The reference cases are also compared to FD-π models with several different numbers of cascaded π-sections n while maintaining a fixed number of parallel branches $m = 5$. The corresponding results in the frequency domain and in the time-domain are reported in Fig. 5 and Fig. 6, respectively. These figures reveal that the number of π-sections n is tightly linked to the maximum frequency range that the model can capture. Thus, a higher value of n is crucial to allow the model to represent fast transients and the high frequency behaviour of the cable. This is confirmed in the time-domain where the
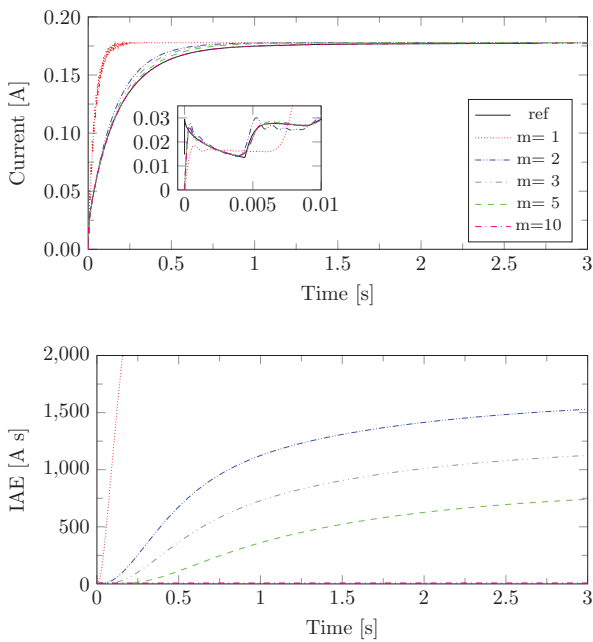
Fig. 4. Comparison of time-domain response for a 400 km XLPE HVDC cable with $n = 10$ FD-π-sections and varying number of parallel branches m.
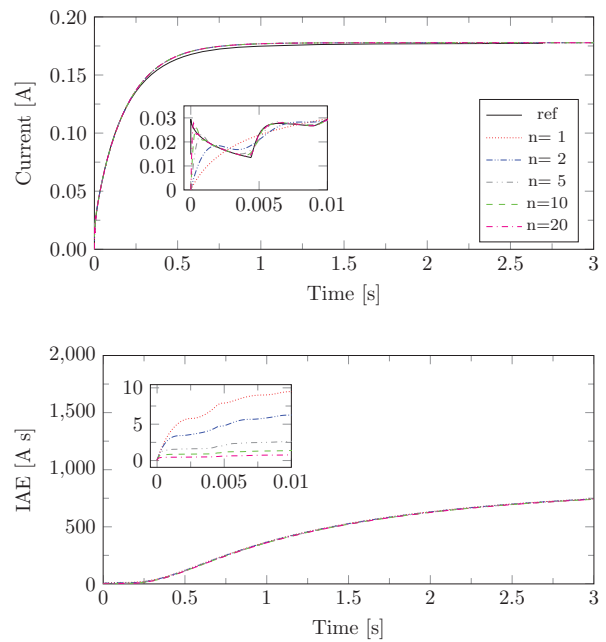

Fig. 5. Cable impedance comparison of a 400 km XLPE VSC HVDC cable for varying number of FD-π-sections n and 5 parallel branches m.

Fig. 6. Time-domain response of a 400 km XLPE VSC HVDC cable for varying number of FD-π-sections n and 5 parallel branches m.
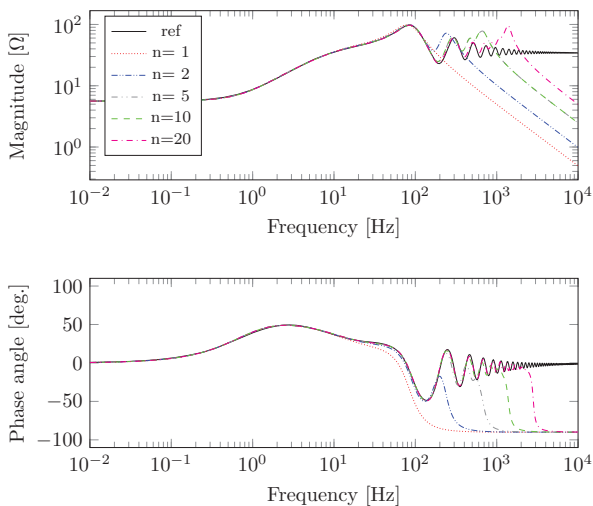
differences between the transient responses, especially for low values of n, are almost negligible in the seconds time range but still noticeable in the first milliseconds.

The presented results show that the use of multiple parallel branches in the FD-π model generally improves the representation of the frequency-dependent behavior of the cable within the lower frequency range. However, independently from the number of parallel branches or π-sections, the FD-π model has a natural limitation for frequencies outside of the model's bandwidth. This can be noticed in Fig. 3 and Fig. 5, where the amplitude of the FD-π model rolls off at high frequencies, while the amplitude of the reference model tends towards a constant value. As discussed in more detail in Section V,

representing the cable correctly in the kHz range implies using a higher order model with an increased bandwidth, which is attained by an increased number of π-sections and, to a lesser extent, an increased number of parallel branches.

It can also be noticed from the figures above that the time-domain results do not directly lead to a simple approach for in-depth model accuracy comparison, since a comparison at a single point in time will not be a suitable general measure of accuracy, while the differences in the IAE are only visible on the short time scale and/or in the steady state. Furthermore, the results can be influenced by the accuracy of the numerical method used to solve the differential equations of the model.

B. Impact of model configuration on eigenvalues of cable state-space models

The lumped parameter circuit equivalent of an FD-π model shown in Fig. 2 allows a straightforward expression of the model in a linear state-space form, as outlined in Appendix A.2. The eigenvalues of the FD-π cable model presented in the previous subsection are shown in the Fig. 7 and in Fig. 8 for the specified values of m and n, respectively.

It should be noted how the complex conjugate eigenvalues for the configuration with $m = 1$ in Fig. 7 are confined in a limited area close to the imaginary axis compared to the cases with a higher value of m. These eigenvalues correspond to poorly damped oscillations in the dynamic response. Already increasing the value of m to 2 ensures a better damping and values of the oscillation frequencies for the complex conjugate eigenvalues quite close to the cases with higher values of m. With an increasing m, the complex conjugate eigenvalues tend to form two almost straight lines, where the modes with the highest oscillation frequencies will correspond to transients
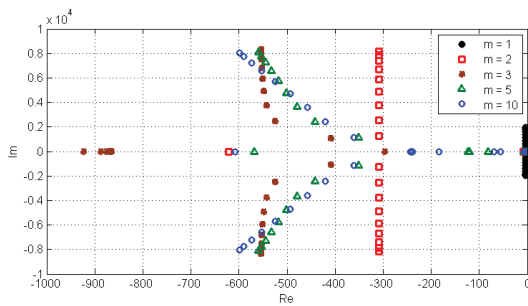
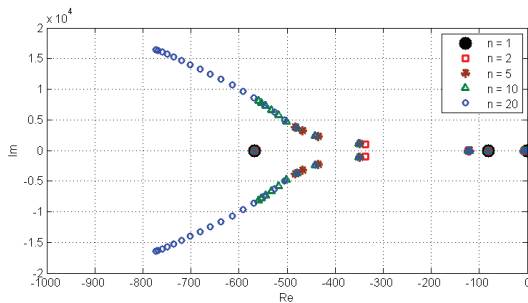Fig. 7. Influence of number of parallel branches m on eigenvalues of state-space model with $n = 10$.

Fig. 8. Influence of number of π-sections n on eigenvalues of state-space model with $m = 5$.

with shorter settling times. The same trend is revealed in Fig. 8 where the increased number of π-sections adds more eigenvalues along these two traces. This fits with the behaviour of the reference model in the frequency domain where the damping of the internal resonances of the cable increases with the frequency. It can also be observed that for higher values of m and n the eigenvalues with lower frequency and lower time constant remain almost in fixed positions while the main variations can be observed for poles characterized by higher oscillation frequency and more negative real parts (i.e. lower time constants). This implies that the changes will affect mostly the fast transients and hence, will be less noticeable in the time-domain response.

IV. MODEL ACCURACY EVALUATION

Considering the expected deviations between the reference model and the FD-π model at very high frequencies, the accuracy should be evaluated within a specified frequency range. Thus, for assessing the accuracy in the frequency domain, a sufficiently wide frequency window to include all the dynamics that can have an effect on the small-signal stability of the HVDC transmission scheme should be defined. Since oscillations with very low frequency can occur in large-scale power systems, the frequency window should span from dc to an upper frequency limit f_B, which should be above the maximum bandwidth of the control systems for the individual HVDC converter terminals.

The accuracy of the model could generally be assessed by calculating an averaged or weighted error over the frequency range of interest. However, the objective of state-space modeling for small-signal stability analysis is typically oriented

towards detecting possible undesired interactions or poorly damped oscillations. Thus, a high error at any frequency of interest might not be acceptable, since it could significantly influence the location of one or more eigenvalues, even if the average error is within a given specification. Hence, the accuracy of the model is assessed in the following by evaluating the maximum error in amplitude and phase within a given frequency range. Specifically, the model accuracy is quantified by the maximum error between the FD-π model and the reference model for the impedance magnitude and phase angle, expressed as:

$$\epsilon_{n,m}^{abs} = \max_{\omega \leq \omega_B} 20 \log_{10} |Z(\omega) - Z_{n,m}(\omega)| \qquad (10)$$

$$\epsilon_{n,m}^{ang} = \max_{\omega \leq \omega_B} |\angle Z(\omega) - \angle Z_{n,m}(\omega)| \qquad (11)$$

where ω_B is the angular frequency (in rad/s) corresponding to the upper frequency limit f_B, Z is the impedance of the reference model and $Z_{n,m}$ the impedance of the FD-π model with n cascaded sections and m parallel branches.

The IAE over a period of 3 seconds is chosen as a relevant metric for assessing the time-domain error.

A. Accuracy evaluation in the frequency domain

The maximum amplitude and phase errors of various FD-π models with different values of m are shown in Fig. 9 as a function of the model order N. The results are shown for a 400 km long cable, with an upper frequency limit f_B set to 500 Hz in order to study typical medium- or low-frequency stability problems below the bandwidth of the converter controls. The case with m=1 is not shown in the figure as the error is always higher than reasonable bounds for the model to be valid.

The results in Fig. 9 confirm that increasing the model order can improve the accuracy and also indicate a pattern in the accuracy associated with the configuration of the model. Indeed, an increasing number of π-sections n as well as a higher number of parallel branches m can improve the model accuracy. It can be observed that for a fixed number of parallel branches $m \geq 3$, increasing the number of cascaded π-sections n and, thus, the order of the model, reduces the error until it reaches an asymptotic value. This asymptotic value decreases with increasing the number of parallel branches m. It should be noted that the curves with lower values for m cross the curves with higher values, which creates a Pareto front of error versus model order. The crossing points indicate when it is preferable to increase the number of parallel branches m, rather than the number of π-sections, to obtain a higher accuracy. For configurations below such crossing points, a lower number of parallel branches m, and consequently a higher number of π-sections n, results in a more accurate model for the same order N.

The results shown in Fig. 9 are obtained with a short-circuited cable, and slightly different curves would result from the same analysis of an open-ended cable, as presented in [26]. In general, the same model configuration will lead to slightly higher maximum errors for short-circuited cables at
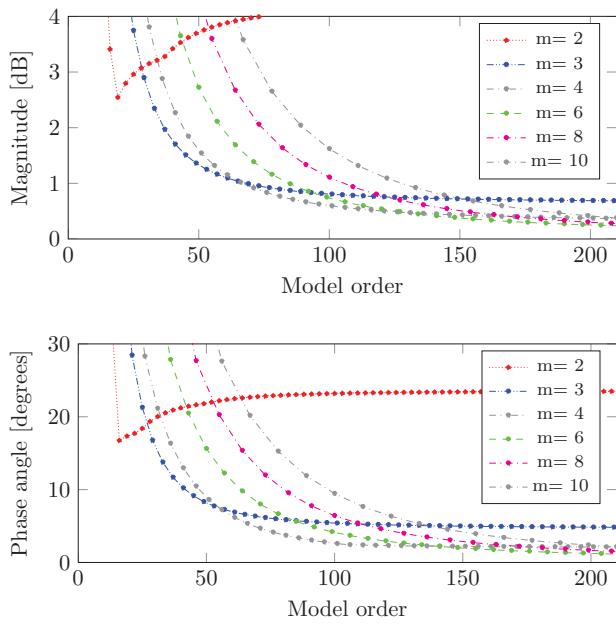
Fig. 9. Maximum amplitude error and phase error in the frequency range below 500 Hz as function of the model order for different number of parallel branches - short-circuited cable termination.
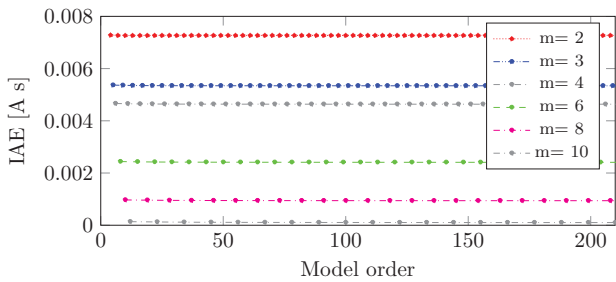

Fig. 10. Overview of IAE as a function of the model order for different number of parallel branches m.

low model orders. Thus, the assumption of a short-circuited cable is suitable as a conservative approach for designing FD-π models within a limited frequency range. However, the open-ended and short-circuited conditions result in approximately the same error for very high model orders. This is reasonable since the validity of a highly accurate cable model should not be dependent on the load impedance.

B. Accuracy evaluation in the time-domain

The IAE for a step response as defined in (9) is evaluated over a period of 3 seconds. This time frame is sufficient to include any noticeable transients, as seen from Fig. 4 and Fig. 6. The obtained results are displayed in Fig. 10 as a function of the model order for several numbers of parallel branches m.

Fig. 10 reveals that the evaluation in the time-domain mainly indicates the accuracy improvement provided by a higher number of parallel branches. Since all the curves appear as almost horizontal lines, they fail to capture the effect of the number of π-sections n at the beginning of the transient.

This behavior is coherent with what has been reported in the previous section, namely that the parameter n acts mostly on the millisecond range. Indeed, the effects of n becomes practically negligible once the error is integrated over time. This implicit bias towards the influence on the slower time response could be corrected by weighting factors or by a logarithmic sampling. Such an approach would correspond to an increased weight for the high-frequency components and would, therefore, reduce the differences compared to the metrics directly defined in the frequency domain. Furthermore, the metrics in the time-domain involve higher computational efforts compared to the metrics in the frequency domain. On this basis, accuracy assessments in the time-domain are discarded when considering methods for optimization of FD-π model configurations.

V. Optimized Model Configurations

The configuration of cable models for small-signal analysis of HVDC transmission systems should be balanced between the two conflicting needs of ensuring a high fidelity within the frequency range of interest while limiting the model complexity. Since the FD-π model offers n and m as two degrees of freedom, the configuration can be subject to optimization. Metrics for quantifying the model fidelity have been introduced in the previous section while the model order can be utilized as a simple scalar indication of the model complexity.

A first natural framework for optimizing the cable model is to identify the configuration with lowest order while imposing a constraint on the model accuracy by specifying the maximum model error over a predefined frequency range. Alternatively, a constraint on the model order could be imposed to limit the model complexity while searching for the configuration ensuring the lowest errors. Both these approaches can be considered as constrained discrete optimization problems in the space of the model configurations. This section presents two algorithms that identify the optimal solution for a specified set of constraints. The obtained solutions correspond to model configurations on the Pareto front representing the minimum achievable error as a function of the model order. The algorithms are both implemented in the accompanying numerical tool.

A. Minimum order configuration with error constraints

The behavior shown in Fig. 9 can be effectively visualized by the Pareto fronts of the model configurations with minimum error as a function of the total model order N. A set of examples for different cable lengths is shown in Fig. 11. The numbers near the markers of each model along the Pareto front report the number of parallel branches m associated with the specific configuration.

The optimization problem of finding the model configuration with the minimum model while respecting maximum error constraints within the specified frequency range can be mathematically expressed as:
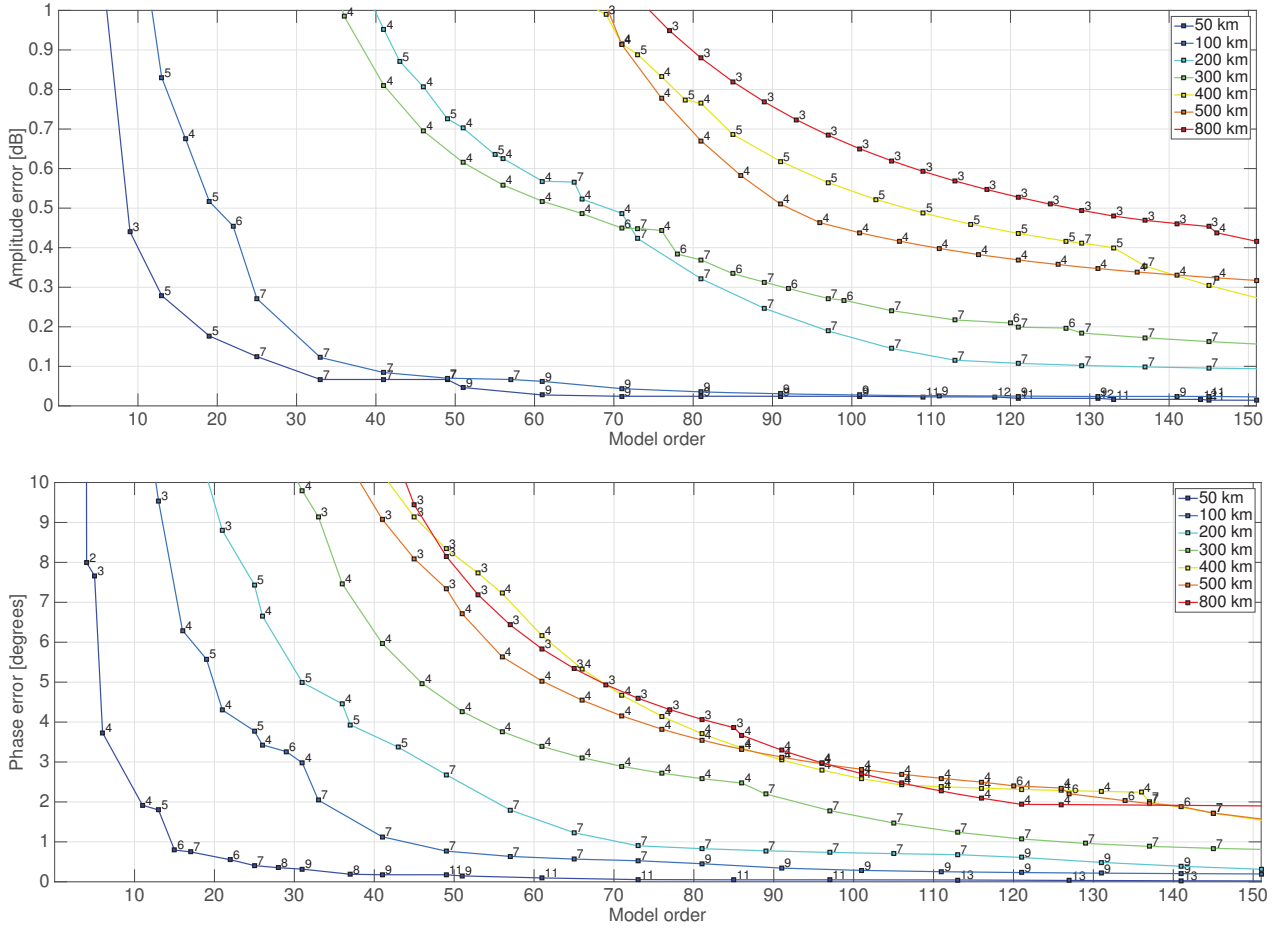
Fig. 11. Amplitude error and phase error for the configuration of minimum order as function of the model order for several cable lengths.

$$\text{minimize } N(n,m), \tag{12}$$

$$\text{subject to } \epsilon^{abs}(n,m) \leq \epsilon^{abs}_{max}, \tag{13}$$

$$\text{and } \epsilon^{ang}(n,m) \leq \epsilon^{ang}_{max}. \tag{14}$$

However, the boundary conditions expressed in (13)–(14) cannot be expressed analytically, as they are defined as single numbers over the predefined frequency range according to (10)–(11). Consequently, a search algorithm is applied in order to find the optimal model configuration.

The conceptual structure of the algorithm proposed for optimizing the configuration of the FD-π model is visualized by the flowchart in Fig. 12. The algorithm starts with the lowest possible order, $N = 3$, which corresponds to a single conventional π section, and is designed to increase the model order until a configuration satisfying the error constraints is identified. As a first step, all the configurations of order N are identified. This corresponds to a search for all the sets of integers n and m satisfying (7). The amplitude and phase errors $\epsilon^{abs}_{n,m}$ and $\epsilon^{ang}_{n,m}$ are calculated for each configuration. If both errors are lower than the specified maximum errors, the associated configuration is considered as a valid solution, otherwise it is discarded. Once all the configurations of order N have been processed, it is verified whether at least one valid

configuration has been identified. In case the analysis results in no valid configuration, the algorithm increments the model order and repeats the procedure. In case more than one valid configuration is detected, the configuration with minimum phase error is selected. It should be noted that typically only one configuration satisfies the constraints and that a different selection criterion would have a very marginal impact on the results.

B. Minimum error configuration with model order constraint

Instead of searching for an optimized model configuration fulfilling an accuracy requirement, it can also be relevant to identify the most accurate model that can be achieved within a predefined model order. The corresponding optimization problem can be mathematically expressed as:

$$\text{minimize } \epsilon^{\chi}(n,m) \text{ with } \chi \in \{abs, ang\} \tag{15}$$

$$\text{subject to } N(n,m) \leq N_{max}, \tag{16}$$

with the function $\epsilon^{\chi}(n,m)$ to be minimized being either $\epsilon^{abs}(n,m)$ or $\epsilon^{ang}(n,m)$ as defined in (10) or (11), respectively.

Since $\epsilon^{\chi}(n,m)$ cannot be written in an analytical form, the most accurate model for a defined maximum order can
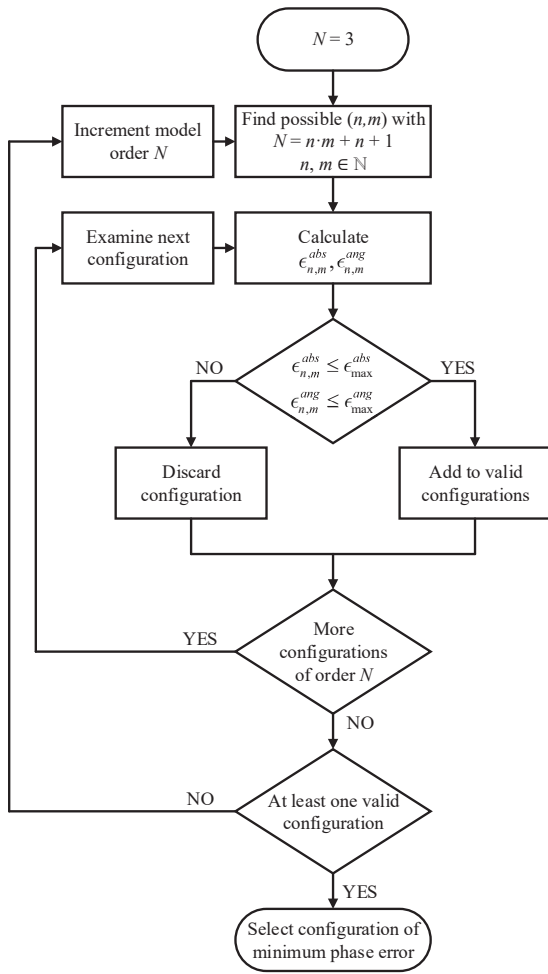
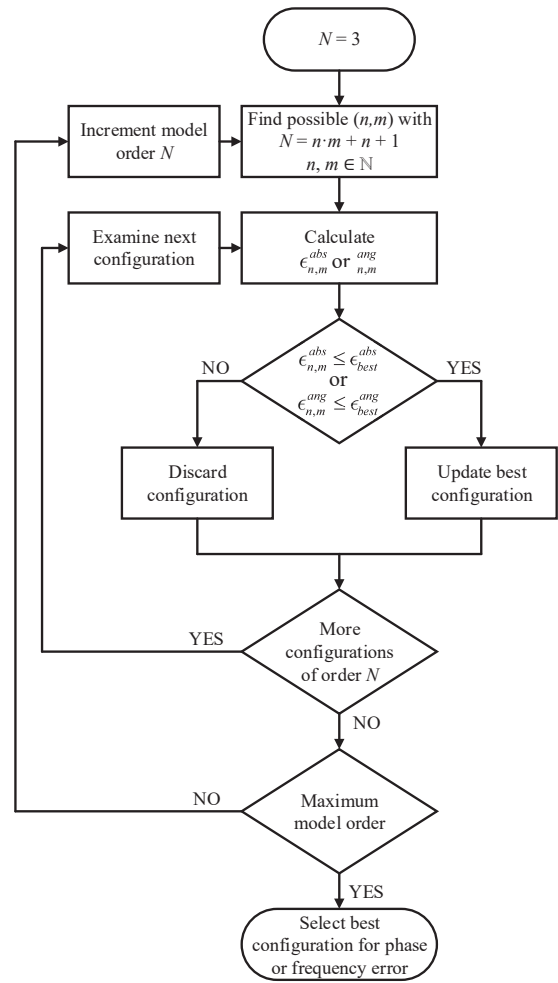Fig. 12. Overview of algorithm for identifying optimal model configuration for a specific accuracy criteria

Fig. 13. Overview of algorithm for identifying optimal model configuration with a specified maximum model order N

again be identified by a search algorithm. The structure of the proposed algorithm is illustrated in Fig. 13. As seen from the figure, the algorithm is starting from the lowest possible model order, $N = 3$, and is increasing the model order until the specified order constraint is reached. For each model order N, all possible configurations are evaluated and their associated errors compared to the error of the most accurate configuration already examined. The most accurate configuration is then continuously updated for each iteration until the maximum model order is reached. This searching procedure is necessary since a configuration with the maximum order will not always provide the most accurate model. Thus, the algorithm follows the Pareto-front of the minimum error until the maximum order is reached, and selects the most accurate available model configuration. As indicated in the flowchart of Fig. 13, it can be specified whether the algorithm should return the solution with the lowest amplitude or phase error in case they occur for different model configurations.

C. Parameter sensitivity analysis

The analysis of the model configuration along the Pareto front in Fig. 11 can be utilized to assess the impact of
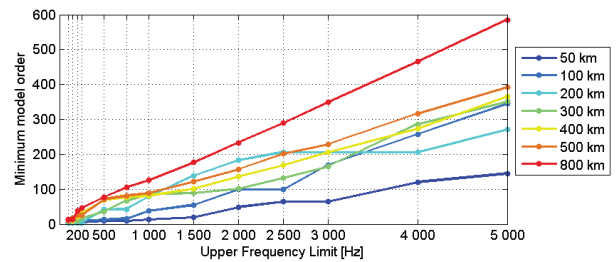

Fig. 14. Minimum model order as function of the upper frequency limit for different cable lengths

parameters such as the cable length, the cable cross section and the upper frequency limit f_B on the optimal model configuration. As an example, the minimum model order as a function of f_B is displayed in Fig. 14 for a set of different cable lengths, with a tolerance on the amplitude error $\epsilon_{n,m}^{abs}$ of 1 dB and a tolerance on the phase error $\epsilon_{n,m}^{ang}$ of 15°. For high values of the upper frequency limit f_B and/or long cables, it can be noticed from the curves in Fig. 14 that the required model order N is increasing approximately linearly with f_B.

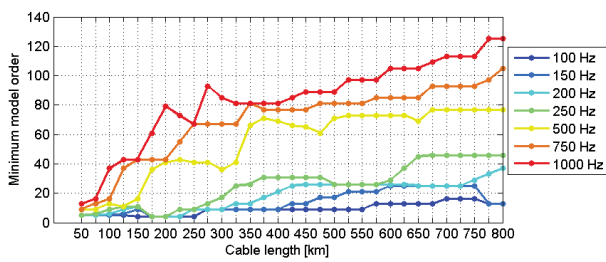In general, the model order is heavily affected by the num-

Fig. 15. Minimum model order as function of cable length for different upper frequency limits f_B

TABLE I
PARAMETERS OF POINT-TO-POINT HVDC TRANSMISSION SYSTEM

Parameter	Value	Parameter	Value
Rated ac voltage	380 kV	P gain $v_{dc,a}$ (2L)	12.0
Rated power	900 MW	I gain $v_{dc,a}$ (2L)	$2.0 * 10^3$
Rated frequency	50 Hz	P gain $v_{dc,a}$ (MMC)	0.882
Dc bus capacitance (2L)	62.7 μ F	I gain $v_{dc,a}$ (MMC)	8.82
P gain $i_{ac,a}$ (2L)	0.174	P gain $i_{ac,b}$	0.209
I gain $i_{ac,a}$ (2L)	0.950	I gain $i_{ac,b}$	1.14
P gain $i_{ac,a}$ (MMC)	0.209	P gain $p_{ac,b}$	0.100
I gain $i_{ac,a}$ (MMC)	1.14	I gain $p_{ac,b}$	40.0

ber of cable resonances falling within the frequency window specified for the evaluation of the model error. Moreover, resonance peaks are shifted to lower frequencies when the cable length is increased. For illustrating this effect, the minimum model order N is plotted as a function of the cable length for various values of f_B in Fig. 15. For high values of f_B, the minimum model order starts increasing noticeably with the cable length when the first cable resonances fall within the frequency window. However, the minimum model order does not increase much with the cable length for very low values of f_B. The reason is that accurate modelling of even the longest cables require only representation of the first resonance peak. After the first resonance peaks have been included in the frequency window of a case with a long cable and/or high values of f_B, increased cable length mainly requires a higher number of π-sections for fulfilling accuracy requirements. Thus, the minimum model order starts increasing linearly with the cable length when f_B and the cable length are above certain values. For such conditions, the general trend of the required model order N can be expressed as:

$$N \propto \ell f_B \qquad (17)$$

Analysing the values of n and m for the results shown in Fig. 14 and Fig. 15 reveals that the configurations on the Pareto fronts with f_B above about 500 Hz are characterized by a higher number of π-sections n compared to shorter cables for the same model order, implying a lower number of parallel branches m [26]. It should also be noted that for long cables, the increase of the model order N is mostly due to the increase in the number of required cascaded π-sections n, while the number of required parallel branches m usually stays between 2 and 5. Indeed, as for traditional phasor-based π-equivalent representation of ac transmission lines, a higher n for longer cables is necessary to achieve a good approximation, due to higher influence of the non-linear hyperbolic terms in (1)–(2).

Another example of how the optimal model configuration is influenced by the system parameters is shown in Fig. 16. In this figure, the axes are defined in logarithmic scale, and the values at the markers for each optimal model configuration indicate the number of parallel branches m. The length of the cable is maintained constant at 400 km, while the cable parameters are changed according to the cross sections given in Table II in the Appendix. From this figure it can be clearly seen that the general trends of the FD-π models at the Pareto front of the model order are relatively similar for different

types of cables. Indeed, all the cable geometries evaluated in Fig. 16 follow a similar trend as shown in linear scale for 400 km of Cable 1 in Fig. 15, with some small individual variations depending on the location of the resonance frequencies of the different cables.

VI. EIGENVALUE-BASED ANALYSIS OF HVDC TRANSMISSION SYSTEM

Two examples of point-to-point HVDC connections with different converter models are evaluated in the following. These examples are presented to illustrate how the cable representation can significantly influence the eigenvalues of a small-signal model of an HVDC transmission system and to demonstrate how results from the presented analysis can be utilized.

The system configuration used for the examples is indicated in Fig. 17. This is a simple point-to-point HVDC transmission system where one converter terminal controls the dc-voltage while the other controls the power flow. For studying the impact of the cable model on different system configurations, the following two different cases are considered: 1) A case where both converters are MMCs represented by the simplified zero-sequence model from [7]. 2) A case where both converters are assumed to be 2L-VSCs represented by traditional average models. It should be noted that these examples are not intended to be a comparison between MMC and 2L VSC point-to-point schemes, but are introduced to highlight the potential consequences of an inadequate cable model. These consequences can range from the presence of poorly damped high frequency oscillations to even instabilities, which a more accurate cable model does not display.

The ratings and main controller parameters of the system are listed in Table I. The control systems and the corresponding small-signal models of the MMCs are the same as in [32], while the models of the 2L VSCs are based on [19]. The main parameters of the system are obtained from [32]. The state equations used for obtaining the evaluated small-signal models are fully documented in Appendix A.2 for the 2L VSCs, and the specific adaptations for modelling of the MMCs are presented in Appendix A.3. For the considered case, the HVDC cable is a 100 km long section of Cable 1 from Table II in Appendix.

The impact of the cable model on the eigenvalues of two different HVDC systems is investigated by considering 4 different model configurations:

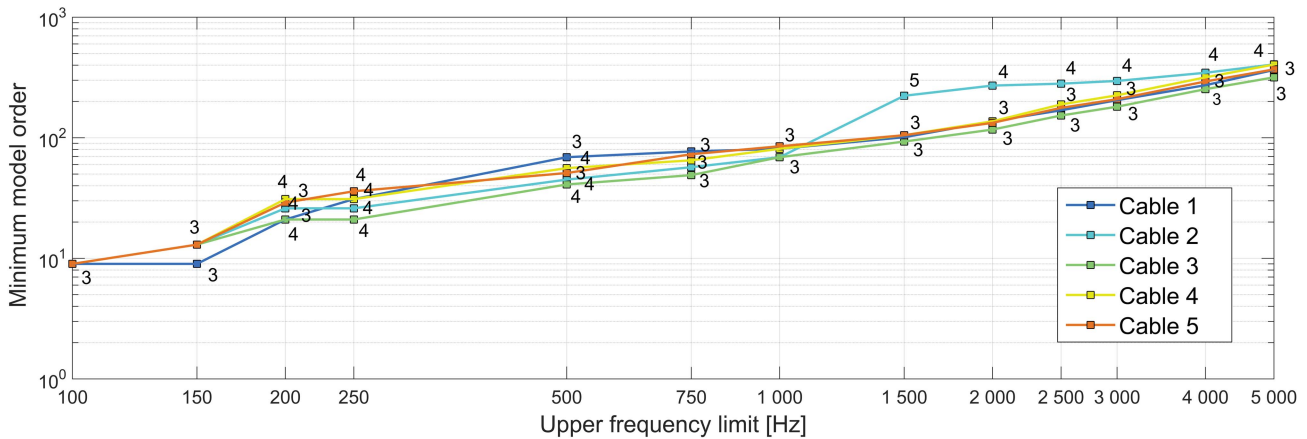(i) A traditional π-model with 15 sections ($m = 1$, $n = 15$)

Fig. 16. Minimum model order as function of the upper frequency limit for 400 km of cable with different cross sections.
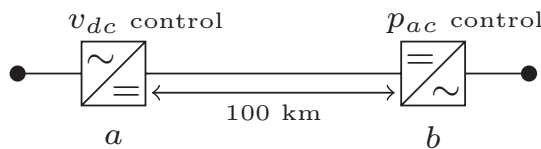

Fig. 17. Example case with point-to-point HVDC transmission system

(ii) An FD-π model with 15 sections and 2 parallel RL-branches per section ($m = 2$, $n = 15$)

(iii) A high-order FD-π model with 15 sections and 10 parallel RL-branches per section ($m = 10$, $n = 15$)

(iv) An optimized FD-π model obtained by the minimum order selection algorithm from Fig. 12

For the optimized FD-π model of case (iv), an upper frequency limit of 500 Hz has been specified, together with a requirement of a maximum amplitude error of $\epsilon_{n,m}^{abs} = 0.5$ dB and a maximum phase error of $\epsilon_{n,m}^{ang} = 5°$. This results in a model with 5 parallel branches and 5 sections ($m = 5$, $n = 5$). It should be noticed that a value of m equal to 5 is in general quite high, but this is a consequence of the relatively short length of the cable and the high accuracy requirements (i.e. the low values of $\epsilon_{n,m}^{abs}$ and $\epsilon_{n,m}^{ang}$).

A. Analysis of system with MMC-based converter terminals

The eigenvalues for the linearized state space model of the MMC-based point-to-point connections with different configurations of the FD-π model is displayed in Fig. 18. As seen from the figure, the system is stable, since all the eigenvalues are located in the left half of the complex plane. However, it can be easily noticed that the lowest order FD-π models are characterized by the presence of poorly damped modes. For the cases with $m = 1$ or $m = 2$, these modes appear along two almost vertical lines with the margin to the stability limit being very low for the case of $m = 1$. For the higher order models, the modes associated to the cables have significantly higher damping and appear on a more diagonal line corresponding to an increased damping and a reduced settling time for
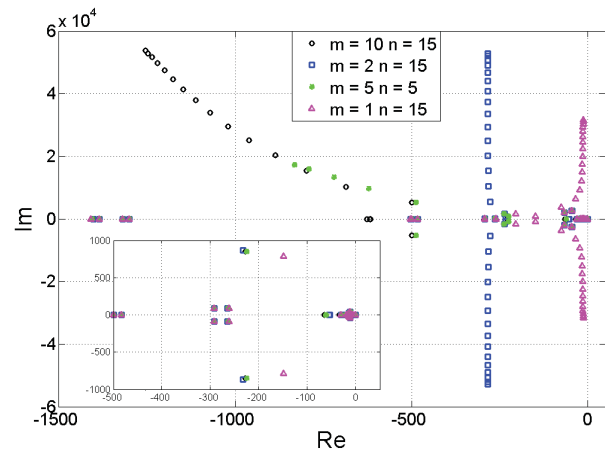

Fig. 18. Comparison of eigenvalues for MMC-based HVDC system with different cable models

the modes with the highest oscillation frequency. The modal analysis indicates that the choice of a low order model in this configuration with MMC terminals does not lead to a wrong stability assessment but could result in poorly damped modes that would be only an artifact of the cable model.

The behavior of the FD-π models evaluated in the previous sub-section has been confirmed with time-domain simulations. As a reference for the time-domain results, the complete model for the point-to-point transmission link has been implemented in the Matlab-Simulink environment and simulated with a fixed time step of 0.5 μs. The cable is represented with a ULM model.

The system starts from steady state and is perturbed at $t = 0$ with a current injection of 0.1 pu imposed directly at the output of the voltage controlling terminal. Results from time-domain simulations showing the response in the dc-voltage at the same terminal with different cable models are presented in Fig. 19. The results confirm that the system is always stable and that all FD-π models behave similarly. However, it can be noticed that the classical π-model presents a high frequency oscillatory
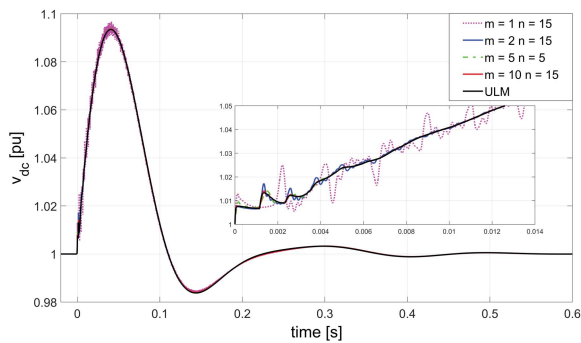
Fig. 19. Verification of small-signal state-space models of MMC HVDC system in comparison to electrical simulation with ULM representing the cable
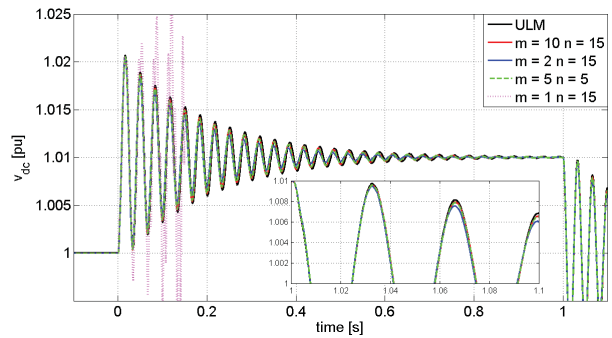

Fig. 21. Verification of small-signal state-space models of 2L VSC HVDC system in comparison to electrical simulation with ULM for representing the cable
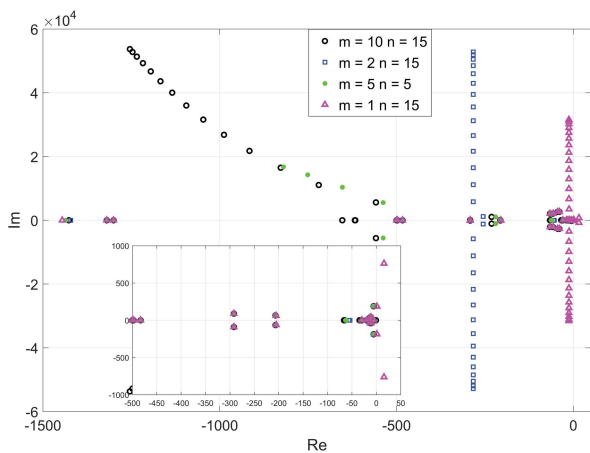

Fig. 20. Comparison of eigenvalues for 2L VSC-based HVDC system with different cable models

mode that dampens in approximately 0.2 s and that is not visible with the other models. This is even more evident in the zoomed figure inset. These oscillatory modes are present also in the eigenvalues of the linearized system that is displayed in Fig. 18 and can be effectively excited during a transient, but do not represent a dynamic behaviour of the actual system.

B. System with 2L VSC terminals

The eigenvalues of the system with converter stations based on 2L VSCs are shown in Fig. 20 for the 4 different cable models. The tuning of the controllers and the configuration have been designed to provide a clear example where the effect of an inadequate cable model can lead to a wrong stability assessment. From the zoomed view in the lower part of the figure, it can be clearly seen that the traditional π-model results in one unstable oscillatory mode at approximately 120 Hz (750 rad/s), which is far away from the eigenvalues of the more accurate cable models. It can also be noted that the system with the traditional π-model presents another unstable mode with an oscillation frequency of 29 Hz (185 rad/s) which is clearly avoided by introducing a more accurate cable model.

From the general overview of the eigenvalues of the HVDC transmission system with the different cable models, it can also

be noticed that the traditional π-model results in excessively low resonant frequencies and low damping ratios for the eigenvalues associated with the cable, as expected from Fig. 3 and Fig. 7. Introducing two parallel branches ensures that false predictions of instability are avoided and that the oscillation frequencies are more accurately represented, even though the damping is still noticeably incorrect for the eigenvalues associated with the cable. The figure also shows that the optimized model (with $m = 5$, $n = 5$) ensures a reasonable approximation of the higher order model (with $m = 10$ and $n = 15$), even if it is not representing the eigenvalues with the highest frequencies that are captured by the more detailed model. However, these high frequency modes are well damped and with short settling times. Moreover, they appear outside the frequency range where interactions with the HVDC control loops are typically to be expected and, hence, of less interest.

Similarly to the MMC case, the modal analysis has been confirmed with time-domain simulations. The system starts from a steady state condition and is perturbed at $t = 0$ with a step of 0.01 pu in the dc voltage reference. The same perturbation is applied to the linearized state-space models of the system. An example of results obtained from all the simulated models is presented in Fig. 21. This figure shows the transient response of the dc bus voltage at the converter controlling the voltage with the response of the reference model plotted in black. In general, the response of the linearized models provides a reasonably accurate representation of the reference model, except for the classical π-model, which is unstable. The frequency of the oscillations is well represented also for the model with $m = 2$ in accordance with the remark of the previous subsections. The results also demonstrate how the optimized FD-π model provides similar accuracy for the dynamics of interest as the more detailed model, but with a significantly lower model order. Thus, false instabilities resulting from the traditional π-model can be avoided while ensuring good accuracy if an appropriately designed FD-π model is utilized.

VII. CONCLUSION

This paper proposes an approach for identifying the most suitable configuration of frequency-dependent π (FD-π) models for representing HVDC cables in small-signal eigenvalue

analysis of HVDC transmission systems. On this basis, two algorithms are presented for finding optimized configurations of FD-π models under constraints on either the model error or the model order. The presented approach and the resulting optimization algorithms are based on studies of the trade-off between accuracy and model order for FD-π models. For this purpose, the accuracy of different FD-π model configurations is evaluated in the frequency-domain and in the time-domain as basis for defining suitable accuracy metrics that can be utilized for identifying the most suitable model configuration for a specific purpose.

The number of parallel branches m and the number of π-sections n fully specify the FD-π model configuration. In general, these two parameters can be associated with a well-distinct role in terms of their physical interpretation. Indeed, the parameter m defines the degree of accuracy in the representation of the frequency dependency of the longitudinal parameters. In principle, a stronger frequency-dependency would require a higher value of this parameter. The parameter n is instead associated with the representation of the travelling waves propagating along the cable. However, the influence of these two parameters on the model accuracy is not fully decoupled when considering a specified accuracy within a frequency range. Thus, separate guidelines for determining n and m independently cannot be generally specified as reliably as the results that can be obtained with the algorithms presented. For long cables and when requiring high accuracy for a large frequency window, the results show that the optimal model order will increase proportionally with the cable length and the upper frequency limit where the accuracy is specified. In practical terms the results indicate that FD-π models with 3 or 4 parallel branches in each section and a number of sections depending on the length of the cable usually provides a good compromise between accuracy and model order.

Examples of small-signal eigenvalue analysis of two different HVDC interconnections are presented to illustrate how an optimized FD-π model can ensure accurate representation of the oscillation modes in the system for cases where too simple models can lead to underestimation of the damping and even false prediction of instability. The presented analysis and the proposed algorithms for identifying optimal FD-π model configurations are developed for HVDC cables, but it is expected that similar methodologies can be developed for HVDC overhead lines as well as for three-phase cables or lines in ac systems.

ACKNOWLEDGMENT

APPENDIX

A.1 Cable parameters

The cross section geometry and the rated voltage of the HVDC cables used for the examples presented in this manuscript are listed in Table II.

TABLE II
CABLE CROSS SECTION DATA

Voltage [kV]	Radius dimension [cm]					
	Core int/ext	Insul.	Sheath	Insul.	Armour	Insul.
1 320	19.5	4.87	5.17	5.47	5.87	6.37
2 400	1.25/3.47	5.72	6.50	7.24	7.81	8.00
3 400	1.25/2.98	4.73	5.36	5.96	6.37	6.60
4 320	2.21	4.86	5.17	5.59	6.19	6.49
5 320	1.67	4.32	4.63	50.5	56.5	6.00

A.2 State-space modelling of HVDC link with 2L VSCs

The state space model of the 2L VSC system used to obtain the small-signal models evaluated in this manuscript are based on the scheme evaluated in [19]. For transparency and reproducibility of the results, the detailed non-linear state-equations of this system are presented in the following. The A- and B-matrices of the small-signal model can be directly obtained by linearization of these equations.

A.2.1.State-space model of 2L VSC with dc voltage control: The state equations for representing the converter terminal operating with dc voltage control are based on the block diagram presented in Fig. 22. It should be noted that all electrical variables (i.e. i_l, v_o and i_o) are represented in the synchronously rotating dq reference frame defined by the PLL. The variables of the electrical system and the control system are indicated in the figure, except for the state variables associated with the PLL, which are defined in Fig. 23 [33]. Thus, the internal state variables of the control systems are mainly $\gamma_{d,q}$ representing the integrator states of the current controllers, κ representing the integrator state of the dc voltage controller, and ϵ representing the integrator of the PI-controller of the PLL. In addition, the control system includes low-pass filters on the measured power and dc voltage ($p_{ac,m}$, $v_{dc,f}$), and a simple algorithm for voltage-based active damping (AD) of LC-filter oscillations, which is based on low-pass filters with states defined as $\phi_{d,q}$. It can be seen from Fig. 22 that the control system for generality includes a power-based droop function in the dc voltage reference, but the droop gain $k_{\delta,p_{ac}}$ is set to zero in the results presented in the manuscript.

For time-invariant modelling of the system, the phase angle between the grid voltage and the reference frame orientation of the PLL must be represented instead of the phase angle θ from the PLL which is used for the reference frame transformations indicated in 22. The state equation defining this relative phase angle displacement is defined as:

$$\dot{\delta\theta} = (\omega_{PLL} - \omega_g)\omega_b \tag{18}$$

Based on the presented figures and considerations, the model of the 2L VSC terminal controlling the dc voltage can be defined by 18 state variables, as listed in the following:

1) $\dot{v}_{o,d} = \dfrac{\omega_b}{c_f}i_{l,d} - \dfrac{\omega_b}{c_f}i_{o,d} + \omega_b\omega_g v_{o,q}$

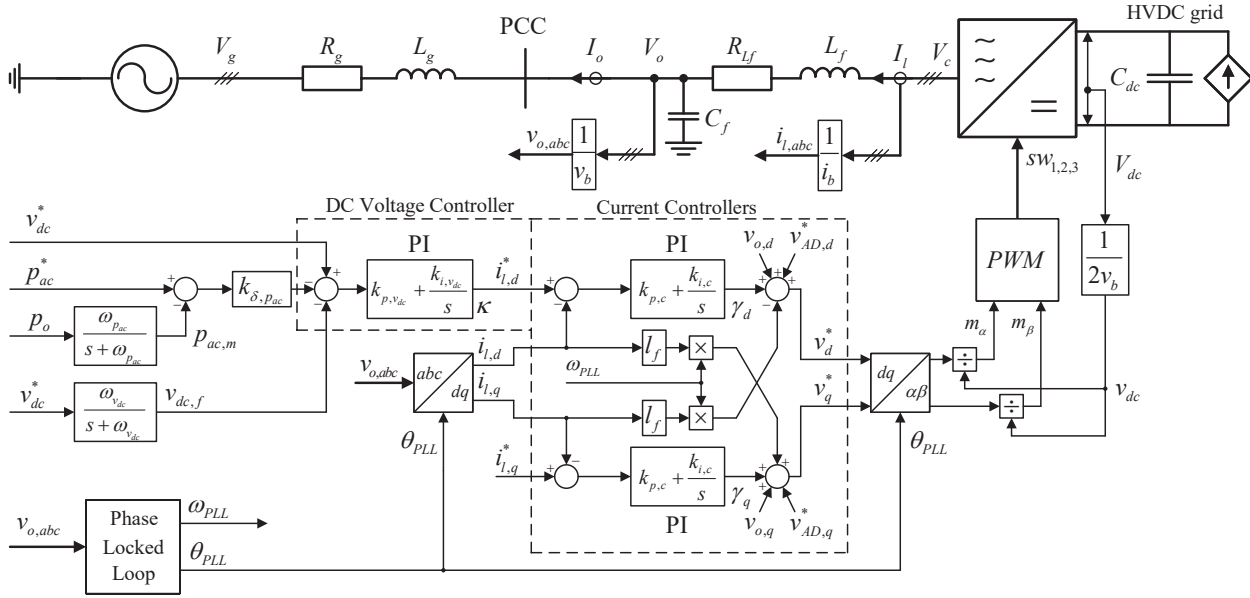2) $\dot{v}_{o,q} = \dfrac{\omega_b}{c_f}i_{l,q} - \dfrac{\omega_b}{c_f}i_{o,q} - \omega_b\omega_g v_{o,d}$

Fig. 22. Overview of control system for 2L VSC with dc voltage control

3) $\dot{i}_{l,d} = -\dfrac{k_{p,c} + r_f}{l_f}\omega_b i_{l,d} - k_{i,PLL}\omega_b \epsilon_{PLL} i_{l,q}$

$\quad - k_{p,PLL}\omega_b \tan^{-1}\left(\dfrac{v_{PLL,q}}{v_{PLL,d}}\right) i_{l,q}$

$\quad - \dfrac{k_{AD} - k_{FF,v} + 1}{l_f}\omega_b v_{o,d} + \dfrac{k_{AD}\omega_b}{l_f}\phi_d$

$\quad + \dfrac{k_{\delta,p_{ac}} k_{p,c} k_{p,v_{dc}}\omega_b}{l_f} p_{ac,m} + \dfrac{k_{i,c}\omega_b}{l_f}\gamma_d$

$\quad - \dfrac{k_{i,v_{dc}} k_{p,c}\omega_b}{l_f}\kappa + \dfrac{k_{p,c} k_{p,v_{dc}}\omega_b}{l_f} v_{dc,f}$

$\quad - \dfrac{k_{p,c} k_{p,v_{dc}}\omega_b (k_{\delta,p_{ac}} p_{ac}^* + v_{dc}^*)}{l_f}$

4) $\dot{i}_{l,q} = k_{i,PLL}\omega_b \epsilon_{PLL} i_{l,d} + k_{p,PLL}\omega_b \tan^{-1}\left(\dfrac{v_{PLL,q}}{v_{PLL,d}}\right) i_{l,d}$

$\quad - \dfrac{k_{p,c} + r_f}{l_f}\omega_b i_{l,q} + \dfrac{i_{l,q}^* k_{p,c}\omega_b}{l_f}$

$\quad - \dfrac{k_{AD} - k_{FF,v} + 1}{l_f}\omega_b v_{o,q} + \dfrac{k_{AD}\omega_b}{l_f}\phi_q + \dfrac{k_{i,c}\omega_b}{l_f}\gamma_q$

5) $\dot{\gamma}_d = -i_{l,d} + k_{\delta,p_{ac}} k_{p,v_{dc}} p_{ac,m} - k_{i,v_{dc}}\kappa$

$\quad + k_{p,v_{dc}} v_{dc,f} - k_{p,v_{dc}}(k_{\delta,p_{ac}} p_{ac}^* + v_{dc}^*)$

6) $\dot{\gamma}_q = -i_{l,q} + i_{l,q}^*$

7) $\dot{i}_{o,d} = -\dfrac{r_g\omega_b}{l_g}i_{o,d} + \omega_b\omega_g i_{o,q}$

$\quad - \dfrac{\hat{v}_g\omega_b}{l_g}\cos(\delta\theta_{PLL}) + \dfrac{\omega_b}{l_g} v_{o,d}$

8) $\dot{i}_{o,q} = -\omega_b\omega_g i_{o,d} - \dfrac{r_g\omega_b}{l_g}i_{o,q}$

$\quad + \dfrac{\hat{v}_g\omega_b}{l_g}\sin(\delta\theta_{PLL}) + \dfrac{\omega_b}{l_g} v_{o,q}$

9) $\dot{\phi}_d = \omega_{AD} v_{o,d} - \omega_{AD}\phi_d$

10) $\dot{\phi}_q = \omega_{AD} v_{o,q} - \omega_{AD}\phi_q$

11) $\dot{v}_{PLL,d} = \omega_{LP,PLL} v_{o,d} - v_{PLL,d}\omega_{LP,PLL}$

12) $\dot{v}_{PLL,q} = \omega_{LP,PLL} v_{o,q} - \omega_{LP,PLL} v_{PLL,q}$

13) $\dot{\epsilon}_{PLL} = \tan^{-1}\left(\dfrac{v_{PLL,q}}{v_{PLL,d}}\right)$

14) $\dot{\delta\theta}_{PLL} = k_{i,PLL}\omega_b \epsilon_{PLL} + k_{p,PLL}\omega_b \tan^{-1}\left(\dfrac{v_{PLL,q}}{v_{PLL,d}}\right)$

15) $\dot{v}_{dc} = \dfrac{k_{p,c}\omega_b}{c_{dc} v_{dc}}i_{l,d}^2 - \dfrac{k_{AD}\phi_d}{c_{dc} v_{dc}}\omega_b i_{l,d}$

$\quad - \dfrac{k_{p,c} k_{p,v_{dc}} k_{\delta,p_{ac}}(p_{ac,m} - p_{ac}^*)}{c_{dc} v_{dc}}\omega_b i_{l,d}$

$\quad - \dfrac{k_{p,c} k_{p,v_{dc}}(v_{dc,f} - v_{dc}^*) - k_{p,c} k_{i,v_{dc}}\kappa}{c_{dc} v_{dc}}\omega_b i_{l,d}$

$\quad - \dfrac{k_{i,c}\gamma_d}{c_{dc} v_{dc}}\omega_b i_{l,d} + \dfrac{k_{AD} - k_{FF,v}}{c_{dc} v_{dc}}\omega_b i_{l,d} v_{o,d}$

$\quad + \dfrac{k_{p,c}\omega_b}{c_{dc} v_{dc}}i_{l,q}^2 - \dfrac{k_{p,c} i_{l,q}^* + k_{AD}\phi_q + k_{i,c}\gamma_q}{c_{dc} v_{dc}}\omega_b i_{l,q}$

$\quad + \dfrac{k_{AD} - k_{FF,v}}{c_{dc} v_{dc}}\omega_b i_{l,q} v_{o,q} + \dfrac{\omega_b}{c_{dc}}i_{dc,s}$

16) $\dot{v}_{dc,f} = \omega_{v_{dc}} v_{dc} - \omega_{v_{dc}} v_{dc,f}$

17) $\dot{\kappa} = -k_{\delta,p_{ac}} p_{ac,m} - v_{dc,f} + k_{\delta,p_{ac}} p_{ac}^* + v_{dc}^*$

18) $\dot{p}_{ac,m} = \omega_{p_{ac}} i_{l,d} v_{o,d} + \omega_{p_{ac}} i_{l,q} v_{o,q} - \omega_{p_{ac}} p_{ac,m}$

A.2.2.State-space model of 2L VSC with ac-side power control: The structure of the control system for the power-controlled converter terminal is the same as for the dc-voltage controlled terminal from Fig. 22. Thus, the main difference
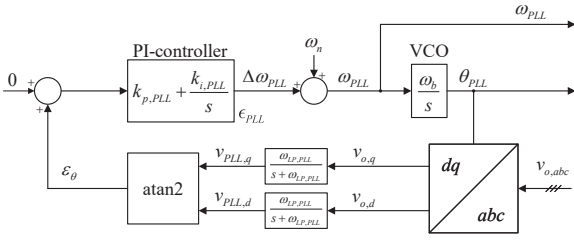
Fig. 23. Structure of the applied Phase Locked Loop

is that an active power controller instead of a dc-voltage controller is providing the d-axis current reference. A dc-voltage droop equivalent to the ac power droop shown in Fig. 22 is also included in the control system for generality. The integrator state of the PI-controller used to regulate the ac power flow is in this case labelled as κ, and the dc voltage droop gain is labelled as $k_{\delta,v_{dc}}$.

Most of the state equations for modelling the converter terminal with ac power control are the same as for the dc-voltage controlled terminal, except for the states that are influenced by the ac power controller. Thus, only the state equations that are different from the model of the dc-voltage controlled converter terminal are listed in the following:

3) $\dot{i}_{l,d} = -\dfrac{k_{p,c} + r_f}{l_f}\omega_b i_{l,d} - k_{i,PLL}\omega_b \epsilon_{PLL} i_{l,q}$

$\qquad - k_{p,PLL}\omega_b \tan^{-1}\left(\dfrac{v_{PLL,q}}{v_{PLL,d}}\right)i_{l,q}$

$\qquad - \dfrac{k_{AD} - k_{FF,v} + 1}{l_f}\omega_b v_{o,d} + \dfrac{k_{AD}\omega_b}{l_f}\phi_d$

$\qquad - \dfrac{k_{\delta,v_{dc}}k_{p,c}k_{p,p_{ac}}}{l_f}\omega_b v_{dc,f} + \dfrac{k_{i,c}\omega_b}{l_f}\gamma_d$

$\qquad + \dfrac{k_{i,p_{ac}}k_{p,c}\omega_b}{l_f}\rho - \dfrac{k_{p,c}k_{p,p_{ac}}\omega_b}{l_f}p_{ac,m}$

$\qquad + \dfrac{k_{p,c}k_{p,p_{ac}}(k_{\delta,v_{dc}}v_{dc}^* + p_{ac}^*)\omega_b}{l_f}$

5) $\dot{\gamma}_d = -i_{l,d} - k_{\delta,v_{dc}}k_{p,p_{ac}}v_{dc,f} + k_{i,p_{ac}}\rho$

$\qquad - k_{p,p_{ac}}p_{ac,m} + k_{p,p_{ac}}(k_{\delta,v_{dc}}v_{dc}^* + p_{ac}^*)$

15) $\dot{v}_{dc} = \dfrac{k_{p,c}\omega_b}{c_{dc}v_{dc}}i_{l,d}{}^2 - \dfrac{k_{AD}\phi_d}{c_{dc}v_{dc}}\omega_b i_{l,d}$

$\qquad - \dfrac{k_{p,c}k_{p,p_{ac}}k_{\delta,v_{dc}}(v_{dc}^* - v_{dc,f})}{c_{dc}v_{dc}}\omega_b i_{l,d}$

$\qquad - \dfrac{k_{p,c}k_{p,p_{ac}}(p_{ac}^* - p_{ac,m})}{c_{dc}v_{dc}}\omega_b i_{l,d}$

$\qquad - \dfrac{k_{i,p_{ac}}\rho + k_{i,c}\gamma_d}{c_{dc}v_{dc}}\omega_b i_{l,d} + \dfrac{k_{AD} - k_{FF,v}}{c_{dc}v_{dc}}\omega_b i_{l,d}v_{o,d}$

$\qquad + \dfrac{k_{p,c}\omega_b}{c_{dc}v_{dc}}i_{l,q}{}^2 - \dfrac{k_{p,c}i_{l,q}^* + k_{AD}\phi_q + k_{i,c}\gamma_q}{c_{dc}v_{dc}}\omega_b i_{l,q}$

$\qquad + \dfrac{k_{AD} - k_{FF,v}}{c_{dc}v_{dc}}\omega_b i_{l,q}v_{o,q} + \dfrac{\omega_b}{c_{dc}}i_{dc,s}$

17) $\dot{\rho} = -p_{ac,m} - k_{\delta,v_{dc}}v_{dc,f} + p_{ac}^* + k_{\delta,v_{dc}}v_{dc}^*$

A.2.3.State-space model of the FD-π cable model: A main feature of the FD-π model is its representation with a lumped circuit as shown in Fig. 2. For the model configuration studied in this paper, it should be noted that the equivalent capacitance $\frac{C}{2}$ at the the cable ends is directly added to the dc-side capacitance of the corresponding converter terminal. Thus, the inputs to the cable model will be the voltages v_{in} and v_{out}. From inspection of the circuit, the model can be directly formulated on general state space form as:

$$\dot{i}_{1,j} = \frac{1}{L_j}(v_{in} - v_1 - R_j i_{1,j}), \qquad \forall\, j : 1 \le j \le m$$

$$\dot{i}_{i,j} = \frac{1}{L_j}(v_{i-1} - v_i - R_j i_{i,j}),$$

$$\qquad \forall\, i : 2 \le i \le n-1, \qquad \forall\, j : 1 \le j \le m$$

$$\dot{i}_{n,j} = \frac{1}{L_j}(v_{n-1} - v_{out} - R_j i_{n-1,j}), \qquad \forall\, j : 1 \le j \le m$$

$$\dot{v}_i = \frac{1}{C}\sum_{j=1}^{m}(i_{i,j} - i_{i+1,j}) - \frac{G}{C}v_i, \qquad \forall\, i : 1 \le i \le n-1$$

A.2.4.Interconnection of models: For interconnecting the converter models and the cable model listed in the previous sections, the dc-side terminals of the converters must be associated to the cable terminals. In this case, we define $v_{dc,1} = v_{in}$ and $v_{dc,2} = v_{out}$, where "1" refers to the dc voltage controlled terminal while "2" refers to the power controlled terminal. Finally the sum of the inductor currents in the parallel RL-branches at the end sections of the cable must be equaled to the dc-side currents for the corresponding converters. Thus, the models are interconnected by defining:

$$i_{dc,s,1} = -\sum_{j=1}^{m} i_{1,j}$$

$$i_{dc,s,2} = \sum_{j=1}^{m} i_{n,j}$$

A.3 State-space modelling of HVDC link with MMCs

The same general control structure is assumed for the MMC-based converter terminals as for the 2L VSCs. For simplicity, also the ac-side model is considered identical, although with different parameters. Thus, the main differences compared to the 2L VSCs is the dc-side interface and the internal dynamics of the MMC. For the purpose of the analysis presented in this paper, a simplified model of the MMC as proposed in [7], [10] is suitable. This applied model represents only the zero sequence dynamics of the total energy (w_Σ) stored in the MMC and the zero sequence circulating current ($i_{c,z}$) which is equal to the current at the dc terminals, and the corresponding control loops.

An overview of the control structure assumed for the MMC-based terminals is shown in Fig. 24. This figure shows that a control loop for the total sum energy is assumed to provide the zero sequence circulating current reference $i_{c,a}^*$.
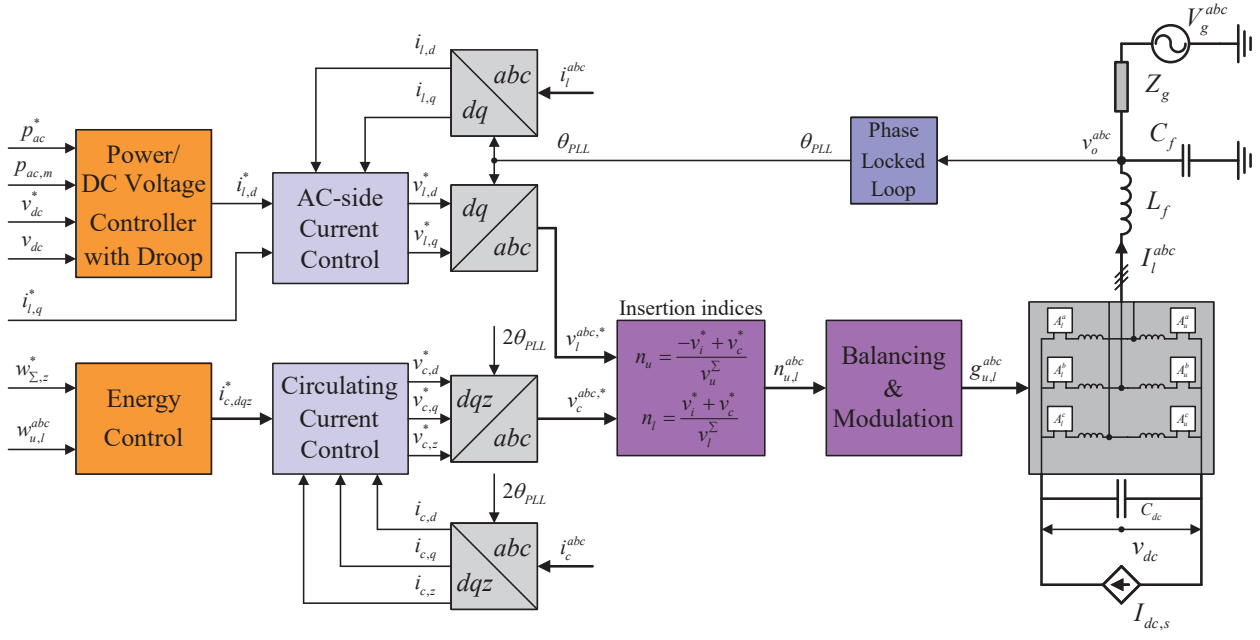
Fig. 24. General overview of assumed control system for MMC-based converter terminals

A circulating current controller is also included, but under the assumptions introduced in [7], [10], only representation of the zero sequence circulating current control is necessary to obtain an accurate model of the dynamic behavior at the ac- and dc-side terminals. When applying PI-controllers for the sum energy and the zero sequence circulating current, the MMC model will include four additional states compared to the equivalent models of the 2L VSC terminals. In the following only these four additional state equations and the equations that are influenced by these states are presented to document the state-space models of the MMC-based HVDC converter terminals. Indeed, all the other state equations are identical to the equations presented for the corresponding 2L VSC cases.

A.3.1 State-space model of a MMC with dc-side voltage control: For the MMC terminal with dc voltage control, the following equations differ from the model already presented for the equivalent 2L VSC:

15) $\dot{v}_{dc} = -\dfrac{\omega_b}{c_{dc}}(4i_{c,z} - i_{dc,s})$

19) $\dot{i}_{c,z} = -\dfrac{k_{p,c_z} + r_a}{l_a}\omega_b i_{c,z} + \dfrac{1 - k_{FF,dc}}{l_a}\omega_b v_{dc}$
$\qquad + \dfrac{k_{i,c_z}\omega_b}{l_a}\xi_z + \dfrac{k_{i,w_{\Sigma,z}}k_{p,c_z}\omega_b}{l_a}\kappa_\Sigma$
$\qquad - \dfrac{k_{p,c_z}k_{p,w_{\Sigma,z}}\omega_b}{l_a}(w_{\Sigma,z} - w_{\Sigma,z}^*)$

20) $\dot{w}_{\Sigma,z} = \dfrac{k_{p,c_z}\omega_b}{2c_{eq}}i_{c,z}{}^2 + \dfrac{k_{FF,dc}\omega_b}{2c_{eq}}i_{c,z}v_{dc}$
$\qquad + \dfrac{k_{p,c_z}(k_{p,w_{\Sigma,z}}(w_{\Sigma,z} - w_{\Sigma,z}^*) - k_{i,w_{\Sigma,z}}\kappa_\Sigma)}{2c_{eq}}i_{c,z}\omega_b$
$\qquad - \dfrac{k_{i,c_z}\xi_z}{2c_{eq}}i_{c,z}\omega_b + \dfrac{k_{p,c}\omega_b}{8c_{eq}}i_{l,d}{}^2$
$\qquad - \dfrac{k_{AD}\phi_d + k_{\delta,p_{ac}}k_{p,c}k_{p,v_{dc}}(p_{ac,m} - p_{ac}^*)}{8c_{eq}}\omega_b i_{l,d}$
$\qquad - \dfrac{k_{i,c}\gamma_d - k_{p,c}k_{i,v_{dc}}\kappa}{8c_{eq}}\omega_b i_{l,d}$
$\qquad + \dfrac{k_{p,c}k_{p,v_{dc}}(v_{dc}^* - v_{dc,f})}{8c_{eq}}\omega_b i_{l,d}$
$\qquad + \dfrac{i_{l,d}v_{o,d}\omega_b(k_{AD} - k_{FF,v})}{8c_{eq}} + \dfrac{k_{p,c}\omega_b}{8c_{eq}}i_{l,q}{}^2$
$\qquad + \dfrac{k_{AD}(v_{o,q} - \phi_q) - k_{FF,v}v_{o,q}}{8c_{eq}}\omega_b i_{l,q}$
$\qquad - \dfrac{k_{p,c}i_{l,q}^* + k_{i,c}\gamma_q}{8c_{eq}}\omega_b i_{l,q}$

21) $\dot{\kappa}_\Sigma = -w_{\Sigma,z} + w_{\Sigma,z}^*$

22) $\dot{\xi}_z = -i_{c,z} + \kappa_\Sigma k_{i,w_{\Sigma,z}} - k_{p,w_{\Sigma,z}}(w_{\Sigma,z} - w_{\Sigma,z}^*)$

It can be noted that the interconnection with the cable model is identical to what is already described for the 2L VSC. However, since the MMC can be operated without an explicit dc-side capacitor, the equivalent value of c_{dc} will be much smaller than for the 2L VSC. Thus, the equivalent capacitance of the cable model, which should be included in c_{dc} as explained in section A.2.3 and A.2.4, can become the

dominant capacitance on at the dc terminals of the converter station.

A.3.2 State-space model of a MMC with ac-side power control: For the MMC with ac-side power control, the only state equation that will be different from the previous cases is the dynamic equation for the total sum energy. This equation is given as:

$$
20)\ \dot{w}_\Sigma = \frac{i_{c,z}{}^2 k_{p,c_z}\omega_b}{2c_{eq}} + \frac{i_{c,z}k_{FF,dc}v_{dc}\omega_b}{2c_{eq}}
$$
$$
+ \frac{k_{p,c_z}\left(k_{p,w_{\Sigma,z}}(w_{\Sigma,z}-w_{\Sigma,z}^*)-\kappa_\Sigma k_{i,w_{\Sigma,z}}\right)}{2c_{eq}}\omega_b i_{c,z}
$$
$$
- \frac{k_{i,c_z}\xi_z}{2c_{eq}}\omega_b i_{c,z} + \frac{i_{l,d}{}^2 k_{p,c}\omega_b}{8c_{eq}} - \frac{i_{l,d}\omega_b k_{AD}\phi_d}{8c_{eq}}
$$
$$
- \frac{i_{l,d}\omega_b k_{p,c}k_{p,p_{ac}}k_{\delta,v_{dc}}(v_{dc}^*-v_{dc,f})}{8c_{eq}}
$$
$$
- \frac{i_{l,d}\omega_b k_{p,c}(p_{ac}^*-p_{ac,m})}{8c_{eq}} - \frac{i_{l,d}\omega_b k_{p,c}k_{i,p_{ac}}\rho}{8c_{eq}}
$$
$$
- \frac{i_{l,d}\omega_b\gamma_d k_{i,c}}{8c_{eq}} + \frac{i_{l,d}v_{o,d}\omega_b(k_{AD}-k_{FF,v})}{8c_{eq}}
$$
$$
+ \frac{i_{l,q}{}^2 k_{p,c}\omega_b}{8c_{eq}} - \frac{i_{l,q}\omega_b(i_{l,q}^*k_{p,c}+k_{AD}\phi_q+\gamma_q k_{i,c})}{8c_{eq}}
$$
$$
+ \frac{i_{l,q}v_{o,q}\omega_b(k_{AD}-k_{FF,v})}{8c_{eq}}
$$

All other equations needed for representing this case are already defined for either the dc-voltage controlled MMC terminal or for presented cases with 2L VSCs.

REFERENCES

[1] D. Van Hertem and M. Ghandhari, "Multi-terminal vsc hvdc for the european supergrid: Obstacles," *Renew. Sustain. Energy Rev.*, vol. 9, no. 9, pp. 3156–3163, Dec. 2010.

[2] N. Chaudhuri, R. Majumder, B. Chaudhuri, and J. Pan, "Stability analysis of VSC MTDC grids connected to multimachine AC systems," *IEEE Trans. Power Del.*, vol. 26, no. 4, pp. 2774–2784, Oct. 2011.

[3] G. O. Kalcon, G. P. Adam, O. Anaya-Lara, S. Lo, and K. Uhlen, "Small-signal stability analysis of multi-terminal VSC-based DC transmission systems," *IEEE Trans. Power Syst.*, vol. 27, no. 4, pp. 1818–1830, Nov. 2012.

[4] J. Beerten, S. D'Arco, and J. A. Suul, "Identification and small-signal analysis of interaction modes in VSC MTDC systems," *IEEE Trans. Power Del.*, vol. 31, no. 2, pp. 888–897, Apr. 2016.

[5] M. Raza, E. Prieto-Araujo, and O. Gomis-Bellmunt, "Small-signal stability analysis of offshore ac network having multiple vsc-hvdc systems," *IEEE Trans. on Power Delivery*, vol. 33, no. 2, pp. 830–839, 4 2018.

[6] A. Jamshidifar and D. Jovcic, "Small-signal dynamic DQ model of modular multilevel converter for system studies," *IEEE Trans. Power Del.*, vol. 31, no. 1, pp. 191–199, Feb 2016.

[7] G. Bergna Diaz, J. A. Suul, and S. D'Arco, "Small-signal state-space modeling of modular multilevel converters for system stability analysis," in *Proc. 2015 IEEE ECCE*, Sept 2015, pp. 5822–5829.

[8] T. Li, A. M. Gole, and C. Zhao, "Harmonic instability in mmc-hvdc converters resulting from internal dynamics," *IEEE Trans. on Power Delivery*, vol. 31, no. 4, pp. 1738–1747, 8 2016.

[9] G. Bergna, J. A. Suul, and S. D'Arco, "State-space modelling of modular multilevel converters for constant variables in steady-state," in *Proc. IEEE COMPEL 2016*, June 2016, pp. 1–9.

[10] G. Bergna-Diaz, J. A. Suul, and S. D'Arco, "Energy-based state-space representation of modular multilevel converters with a constant equilibrium point in steady-state operation," *IEEE Trans. on Power Electronics*, vol. 33, no. 6, pp. 4832–4851, 6 2018.

[11] A. Morched, B. Gustavsen, and M. Tartibi, "A universal model for accurate calculation of electromagnetic transients on overhead lines and underground cables," *IEEE Trans. Power Del.*, vol. 14, no. 3, pp. 1032–1038, Jul. 1999.

[12] W. Wang, M. Barnes, and O. Marjanovic, "Droop control modelling and analysis of multi-terminal VSC-HVDC for offshore wind farms," in *Proc. IET ACDC 2012*, Birmingham, UK, Dec. 4–6, 2012, 6 pages.

[13] W. Wang, M. Barnes, O. Marjanovic, and O. Cwikowski, "Impact of DC breaker systems on multiterminal VSC-HVDC stability," *IEEE Trans. Power Del.*, vol. 31, no. 2, pp. 769–779, Apr. 2016.

[14] G. Pinares, L. Tjernberg, L. A. Tuan, C. Breitholtz, and A.-A. Edris, "On the analysis of the dc dynamics of multi-terminal VSC-HVDC systems using small signal modeling," in *Proc. IEEE PowerTech 2013*, Grenoble, France, Jun. 16-20, 2013, 6 pp.

[15] G. Pinares and M. Bongiorno, "Modeling and analysis of VSC-based HVDC systems for DC network stability studies," *IEEE Trans. Power Del.*, vol. 31, no. 2, pp. 848–856, Apr. 2016.

[16] J. A. Rocendo Macias, A. Gomez Exposito, and A. Bachiller Soler, "A comparison of techniques for state-space transient analysis of transmission lines," *IEEE Trans. Power Del.*, vol. 20, no. 2, pp. 894–903, Apr. 2005.

[17] S. Akkari, E. Prieto-Araujo, J. Dai, O. Gomis-Bellmunt, and X. Guillaud, "Impact of the DC cable models on the SVD analysis of a multi-terminal HVDC system," in *Proc. PSCC*, Genova, Italy, Jun. 20–24, 2016, 6 pp.

[18] P. Rault, "Dynamic modeling and control of multi-terminal HVDC grids," Ph.D. dissertation, Ecole Centrale de Lille, Mar. 2014.

[19] J. Beerten, S. D'Arco, and J. A. Suul, "Frequency-dependent cable modelling for small-signal stability analysis of VSC-HVDC systems," *IET Gener., Transm. Distrib.*, vol. 10, no. 6, pp. 1370–1381, 2016.

[20] C.-S. Yen, Z. Fazarinc, and R. L. Wheeler, "Time-domain skin-effect model for transient analysis of lossy transmission lines," *Proceedings of the IEEE*, vol. 70, no. 7, pp. 750–757, July 1982.

[21] "RSCAD manual – VSC small time-step model," RTDS Technologies, Tech. Rep., Oct. 2006, 136 pages.

[22] J. Beerten, S. D'Arco, and J. A. Suul, "Cable model order reduction for HVDC systems interoperability analysis," in *Proc. IET ACDC 2015*, Birmingham, UK, Feb., 10-12 2015, 10 pages.

[23] F. Thams, S. Chatzivasileiadis, E. Prieto-Araujo, and R. Eriksson, "Disturbance attenuation of dc voltage droop control structures in a multi-terminal HVDC grid," in *In Proc. IEEE PowerTech 2017*, Manchester, UK, June 2017.

[24] J. Freytes, S. Akkari, P. Rault, M. M. Belhaouane, F. Gruson, F. Colas, and X. Guillaud, "Dynamic analysis of MMC-based MTDC grids: Use of MMC energy to improve voltage behavior," *IEEE Transactions on Power Delivery*, vol. 33, no. 1, pp. 429–439, 2018.

[25] J. Sau-Bassols, E. Prieto-Araujo, O. Gomis-Bellmunt, and F. Hassan, "Series interline DC/DC current flow controller for meshed HVDC grids," *IEEE Transactions on Power Delivery*, vol. 33, no. 2, pp. 881–891, April 2018.

[26] S. D'Arco, J. A. Suul, and J. Beerten, "Analysis of accuracy versus model order for frequency-dependent pi-model of HVDC cables," in *Proc. IEEE COMPEL*, Trondheim, Norway, Jun. 27–29 2016, 8 pages.

[27] B. Gustavsen, T. Noda, J. Naredo, F. Uribe, and J. Martinez-Velasco, *Power System Transients: Parameter Determination*. Taylor and Francis Group, 2010, ch. 3, pp. 137–175.

[28] S. Grivet-Talocia and B. Gustavsen, *Passive Macromodelling, Theory and Applications*. Wiley, 2016, ch. 12, pp. 563–661.

[29] P. Moreno and A. Ramirez, "Implementation of the numerical Laplace transform: A review," *IEEE Trans. Power Del.*, vol. 23, no. 4, pp. 2599–2609, Oct. 2008.

[30] B. Gustavsen and A. Semlyen, "Rational approximation of frequency domain responses by vector fitting," *IEEE Trans. Power Del.*, vol. 14, no. 3, pp. 1052–1061, Jul. 1999.

[31] W. Leterme, N. Ahmed, J. Beerten, L. Ängquist, D. Van Hertem, and S. Norrga, "A new HVDC grid test system for HVDC grid dynamics and protection studies in EMT-type software," in *Proc. IET ACDC 2015*, Birmingham, UK, Feb., 10-12 2015, 7 pp.

[32] J. Beerten, G. B. Diaz, S. D'Arco, and J. A. Suul, "Comparison of small-signal dynamics in mmc and two-level vsc hvdc transmission schemes," in *Proc. IEEE Energycon 2016*, Apr., 6-9, pp. 1–9.

[33] S. D'Arco, J. A. Suul, and M. Molinas, "Implementation and analysis of a control scheme for damping of oscillations in vsc-based hvdc grids," in *2014 16th International Power Electronics and Motion Control Conference and Exposition*. IEEE, 2014, pp. 586–593.

Salvatore D'Arco received the M.Sc. and Ph.D. degrees in electrical engineering from the University of Naples "Federico II", Naples, Italy, in 2002 and 2005, respectively. From 2006 to 2007, he was a postdoctoral researcher at the University of South Carolina, Columbia, SC, USA. In 2008, he joined ASML, Veldhoven, the Netherlands, as a Power Electronics Designer, where he worked until 2010. From 2010 to 2012, he was a postdoctoral researcher in the Department of Electric Power Engineering at the Norwegian University of Science and Technology (NTNU), Trondheim, Norway. In 2012, he joined SINTEF Energy Research where he currently works as a Research Scientist. His main research activities are related to control and analysis of power-electronic conversion systems for power system applications, including real-time simulation and rapid prototyping of converter control systems.

Jon Are Suul (M'11) received the M.Sc. degree in energy and environmental engineering and the Ph.D. degree in electric power engineering from the Norwegian University of Science and Technology (NTNU), Trondheim, Norway, in 2006 and 2012, respectively. From 2006 to 2007, he was with SINTEF Energy Research, Trondheim, where he was working with simulation of power electronic converters and marine propulsion systems until starting his PhD studies. From 2012, he resumed a position as a Research Scientist at SINTEF Energy Research, first in part-time position while also working as a part-time postdoctoral researcher at the Department of Electric Power Engineering of NTNU until 2016. Since August 2017, he is also serving as Adjunct Associate Professor at the Department of Engineering Cybernetic of NTNU. His research interests are mainly related to modelling, analysis and control of power electronic converters in power systems, renewable energy applications and for electrification of transport.

Jef Beerten (S'07, M'13, SM'19) received the M.Sc. degree in electrical engineering and a Ph.D. in electrical engineering from the University of Leuven (KU Leuven), Belgium, in 2008 and 2013, respectively. Currently, he is an assistant professor with KU Leuven and EnergyVille. His research interests include future power system dynamics, modeling, and control.

In 2011, he was a visiting researcher at the Royal Institute of Technology (KTH), Stockholm, Sweden, for three months. From April 2014 until March 2015, he was a visiting postdoctoral researcher at the Norwegian University of Science and Technology (NTNU), Trondheim, Norway.

Dr. Beerten was the first winner of the ABB Research Award in Honor of Hubertus von Gruenberg in 2016 and received the KBVE/SRBE Robert Sinave Award and the Prix Paul Caseau from the Institut de France - EDF Foundation for his Ph.D. thesis on modeling and control of DC grids. Dr. Beerten is an active member of both the IEEE and CIGRE.